



# Deep learning-based inpainting of saturation artifacts in optical coherence tomography images

Muyun Hu<sup>\*,§</sup>, Zhuoqun Yuan<sup>\*,§</sup>, Di Yang<sup>\*</sup>, Jingzhu Zhao<sup>†</sup> and Yanmei Liang<sup>Ⓛ<sup>Ⓜ</sup>\*,‡</sup>

*\*Institute of Modern Optics, Nankai University*

*Tianjin Key Laboratory of Micro-scale Optical Information Science and Technology  
Tianjin 300350, China*

*†Department of Thyroid and Neck Tumor*

*Tianjin Medical University Cancer Institute and Hospital*

*National Clinical Research Center for Cancer*

*Key Laboratory of Cancer Prevention and Therapy, Tianjin 300060, China*

*‡ymliang@nankai.edu.cn*

Received 17 August 2023

Accepted 4 October 2023

Published 31 October 2023

Limited by the dynamic range of the detector, saturation artifacts usually occur in optical coherence tomography (OCT) imaging for high scattering media. The available methods are difficult to remove saturation artifacts and restore texture completely in OCT images. We proposed a deep learning-based inpainting method of saturation artifacts in this paper. The generation mechanism of saturation artifacts was analyzed, and experimental and simulated datasets were built based on the mechanism. Enhanced super-resolution generative adversarial networks were trained by the clear-saturated phantom image pairs. The perfect reconstructed results of experimental zebrafish and thyroid OCT images proved its feasibility, strong generalization, and robustness.

*Keywords:* Optical coherence tomography; saturation artifacts; deep learning; image inpainting.

## 1. Introduction

Optical coherence tomography (OCT) acquires information from the surface and interior of the sample by collecting the interference light signals scattered back from the sample, and measurements of back reflection or backscattering versus depth are

known as axial scans (A-scans). OCT has been widely used in the imaging of biological tissues such as eyes,<sup>1,2</sup> skin,<sup>3,4</sup> and cardiovascular.<sup>5,6</sup> As a medical imaging technology, higher image quality has been pursued for OCT. However, during OCT imaging, limited by the dynamic range of the

<sup>‡</sup>Corresponding author.

<sup>§</sup>Muyun Hu and Zhuoqun Yuan contributed equally.

acquisition detector, saturation of the spectral signal often occurs at the point or interface with strong reflection, resulting in streak-like “saturation artifacts” in OCT images after inverse Fourier transformation (IFT). The saturation artifact can be easily produced by excessive light intensity at the focus position of the OCT objective, and is almost unavoidable when the surface of the sample is undulating.<sup>7,8</sup> More importantly, imaging quality and subsequent image processing are seriously affected by saturation artifacts, especially in biological tissues with complicated structures. Therefore, how to remove the saturation artifacts and reconstruct proper signals conveniently and accurately is of great importance for OCT imaging.

Some methods have been proposed to remove saturation artifacts in OCT images. In 2014, Wu *et al.* built a two-level spectral-domain OCT (SD-OCT) system with a dual-line charge-coupled device (CCD) camera<sup>9</sup> to simultaneously acquire two signals from two lines, named line A and line B, and the unsaturated signal was detected by line B to compensate for the saturated signal detected by line A. In 2018, Li *et al.* used a broadband power divider with a ratio of 1:25 to compensate and reconstruct the saturated high-level signal with the low-level signal.<sup>10</sup> The method of reconstructing signals based on power splitting can remove saturation artifacts in OCT images, but the signal compensation may produce large errors at out-of-focus locations, and the hardware changes of the system may limit the practicality of this method due to the cost and technical level.

With the improvement of computational power, some digital image processing-based methods<sup>11</sup> have also been used to remove saturation artifacts in OCT images. In 2012, Huang and Kang fixed saturation artifacts with linear interpolation (LI) of adjacent normal A-scans,<sup>12</sup> but it was not applicable to the case of dense A-scan saturation. In 2021, Liu *et al.* proposed the dictionary-based sparse representation for saturation artifacts inpainting.<sup>13</sup> A generalized dictionary was trained with OCT images from distinct types of samples, but the processed images may be smoothed with the sparsity-based methods and lead to the loss of image details of boundaries.

Because of its superb learning ability and generalization capacity, deep learning has been widely

applied to quality enhancement for OCT images.<sup>14–16</sup> In this study, we proposed a deep learning-based approach to correct OCT images with saturation artifacts. To address this problem, we analyzed the generation mechanism of the saturation artifact in OCT images and designed a data acquisition framework based on the mechanism to construct experimental and simulated datasets separately. Then, enhanced super-resolution generative adversarial networks (ESRGAN)<sup>17</sup> were trained to build artifacts inpainting models. It is demonstrated by the results of zebrafish and human thyroid tissue OCT images that saturation artifacts in OCT images can be effectively corrected by the deep learning method, which proved its great potential in practical application because of its robustness.

## 2. Methods and Materials

### 2.1. Mechanism of the saturation artifact

For studying the generation mechanism of the saturation artifact, the saturation of the OCT signal was simulated with a single scattering point, which is shown in Fig. 1.

We simulated the interference spectrum signal of a Gaussian light source with a central wavelength of 840 nm and a bandwidth of 100 nm under the action of a single scattering point. As shown in Figs. 1(a<sub>1</sub>) and 1(b<sub>1</sub>), when the signal is not saturated, we can only see the direct current (DC) term and the fundamental frequency signal at the scattering point after IFT. However, when the signal is saturated (Fig. 1(a<sub>2</sub>)), it will lead to spectral truncation, and the scattering signals appear at the frequency multiplication positions after IFT (Fig. 1(b<sub>2</sub>)), which means that artifacts will appear at different depths of the OCT image. In actual OCT imaging, the signals of multiple scattering points are intertwined, so they appear as streak-like artifacts in A-scans.

In summary, limited by the dynamic range, when the intensity of the interferometric signal is too strong, the original spectrum will be truncated. Then after IFT, there will be streak-like saturation artifacts in OCT images, appearing as bright short vertical straight lines at the frequency doubling signal.

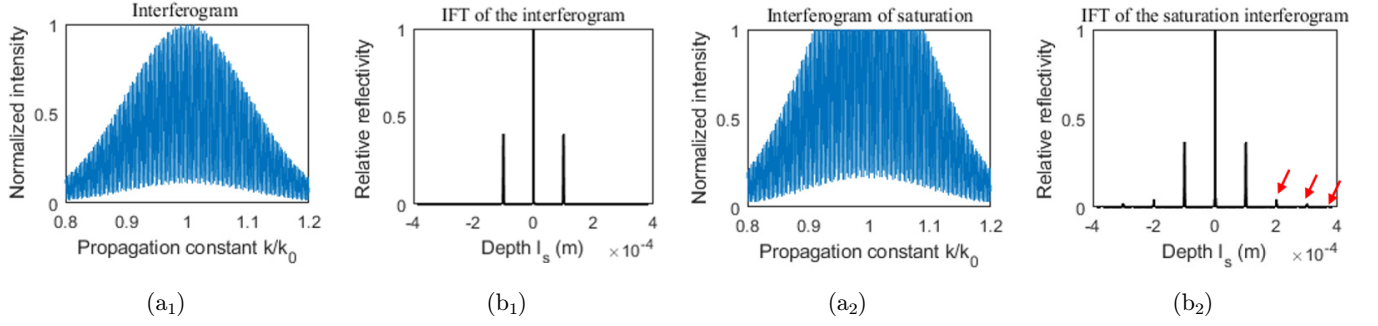


Fig. 1. Simulation of saturation of OCT signal with a single scattering point. (a<sub>1</sub>) Clear interference spectrum signal of a single scattering point. (b<sub>1</sub>) IFT of the signal in (a<sub>1</sub>). (a<sub>2</sub>) Saturated interference spectrum signal of a single scattering point. (b<sub>2</sub>) IFT of the signal in (a<sub>2</sub>).

## 2.2. Construction of artifacts inpainting datasets

Based on the generation mechanism of the saturation artifacts, we used a homemade OCT system<sup>18</sup> to acquire clear-saturated image pairs of the phantom and built experimental and simulated datasets. Among the datasets, clear OCT images were collected by the OCT system, and saturated OCT images were obtained through experiments and simulation separately.

During the construction of experimental datasets, the collected normal OCT image was called the clear image, and the saturated image was collected by enlarging the size of the aperture in the reference arm and called the experimental saturated image. The clear-saturated image pairs acquired by this method were used to build the experimental

dataset. Typical phantom images and A-scan spectral signals in experimental datasets are shown in Fig. 2. Figures 2(a<sub>1</sub>) and 2(a<sub>3</sub>) show the clear image and the experimental saturated image, respectively. Figures 2(a<sub>2</sub>) and 2(a<sub>4</sub>) are one of the typical A-scan spectral signals in the corresponding images, respectively. Compared with the clear image (Fig. 2(a<sub>1</sub>)), streak-like saturation artifacts appear as bright short vertical lines at the frequency-doubling signal in the experimental saturated image (Fig. 2(a<sub>3</sub>)), which is consistent with the generation mechanism of the saturation artifacts. Moreover, the signal intensity of the spectral diagram (Fig. 2(a<sub>4</sub>)) corresponding to the experimental saturated image (Fig. 2(a<sub>3</sub>)) is stronger, which is related to the enhanced intensity of the interference signal and background spectrum when enlarging the aperture of the reference arm.

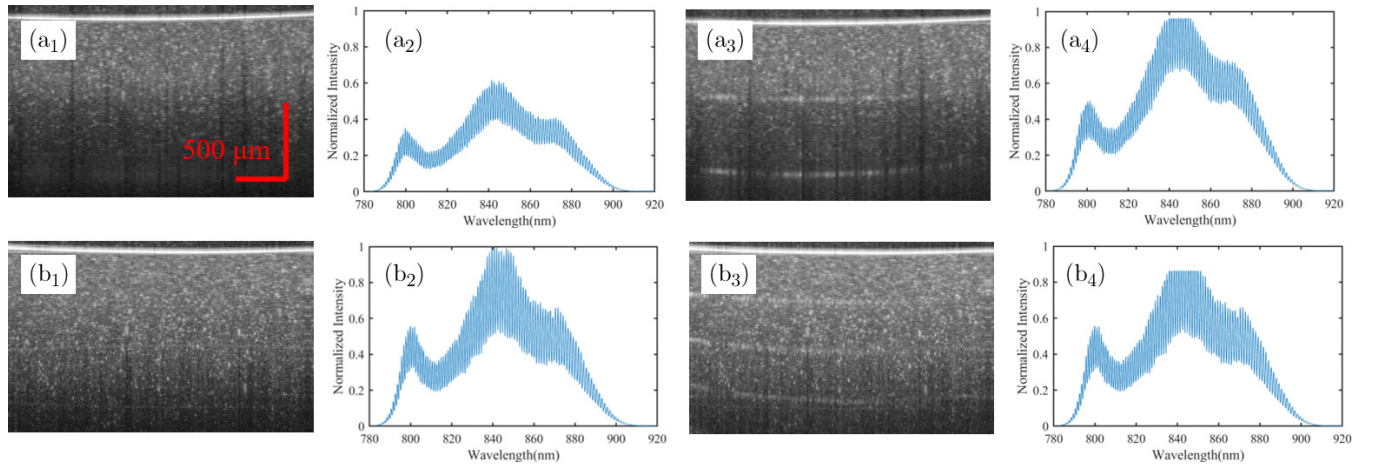


Fig. 2. Comparison of typical clear and saturated phantom images and A-scan spectral signals. (a<sub>1</sub>) is the clear image in experimental datasets. (a<sub>2</sub>) is an A-scan spectral signal diagram of (a<sub>1</sub>). (a<sub>3</sub>) is the experimental saturated image. (a<sub>4</sub>) is an A-scan spectral signal diagram of (a<sub>3</sub>). (b<sub>1</sub>) is the clear image in simulated datasets. (b<sub>2</sub>) is an A-scan spectral signal diagram of (b<sub>1</sub>). (b<sub>3</sub>) is the simulated saturated image. (b<sub>4</sub>) is an A-scan spectral signal diagram of (b<sub>3</sub>).

For the clear image collected experimentally, we generated its saturated image based on the generation mechanism of saturation artifacts, which was called the simulated saturated image. Figures 2(b<sub>1</sub>)–2(b<sub>4</sub>) show the typical OCT image pair and A-scan spectral signals in simulated datasets. Figure 2(b<sub>1</sub>) is the collected clear image and Fig. 2(b<sub>2</sub>) is one of its typical A-scan spectral signals. Figure 2(b<sub>3</sub>) is the generated simulated saturated image, and Fig. 2(b<sub>4</sub>) is the simulated spectral signal of Fig. 2(b<sub>3</sub>).

We introduced the artificial saturation threshold during the generation of simulated saturated images. For each A-scan signal,  $I_{\text{mean}} \times k$  is set as the saturation threshold, and the pixel value exceeding this threshold is equal to the saturation threshold. Among them,  $I_{\text{mean}}$  is the average signal intensity, and  $k$  is the saturation threshold coefficient. After thresholding the original spectrum, an image with saturation artifacts was generated by IFT, and the value of coefficient  $k$  can be adjusted according to the visual effect of the image. Similar to the experimental saturated image (Fig. 2(a<sub>3</sub>)), we can see that streak-like saturation artifacts occur in the simulated saturated image (Fig. 2(b<sub>3</sub>)).

As shown in the two kinds of saturated OCT images in Fig. 2, the saturation artifacts have the same characteristics, bright vertical straight lines at different depths produced from the strong reflective

signal of the phantom surface, which introduce pseudo-signal and mask the micro-structure of the corresponding positions.

### 2.3. Networks

After acquiring the image pairs, generative adversarial networks were trained to learn the correspondence of the clear–saturated image pairs.

During training, the saturated OCT images were input into the network, and their corresponding clear images were target images or ground truth (GT) images. During the inpainting process, the saturated OCT image was input into the trained model to reconstruct the OCT image. In the study, the experimental and simulated datasets were used to train two neural networks, and were named as the experimental and simulated artifacts inpainting models, respectively.

ESRGAN<sup>17</sup> has been used in image super-resolution,<sup>19</sup> image denoising,<sup>20</sup> and image defogging.<sup>21</sup> It achieved better results than other networks and had excellent visual effect. Therefore, we adopted it to evaluate the effect of deep learning on saturation artifacts inpainting in our study.

The network structures are shown in Fig. 3. ESRGAN is composed of a generator and a discriminator. The residual-in-residual dense blocks (RRDB) are used in the generator as the basic

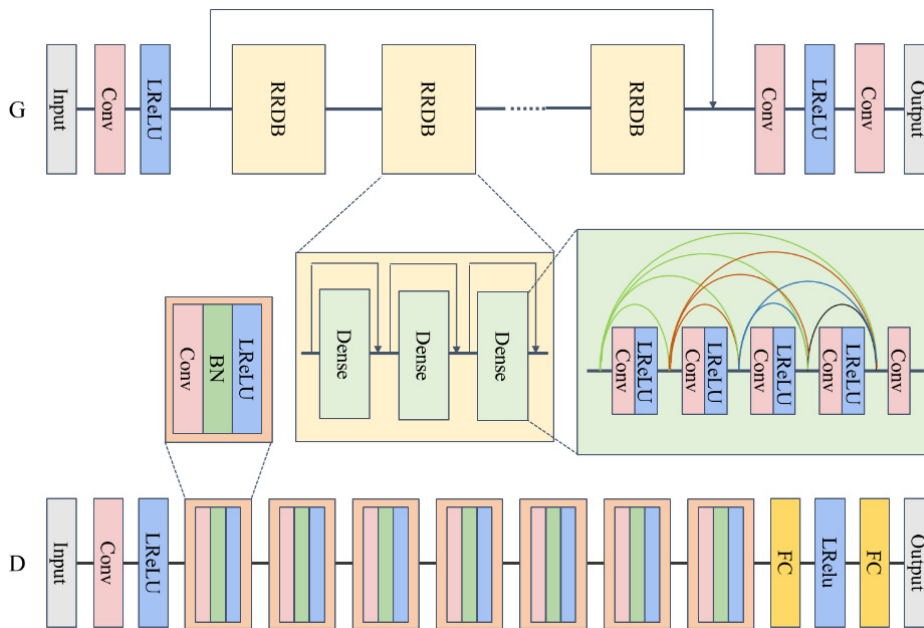


Fig. 3. Network architectures. G: generator. D: discriminator.

building block. The dense block is a DenseNet structure constructed by five convolutional layers (Conv) and three dense blocks are combined with residual connections to construct an RRDB structure. The up-sampling module of the network was removed because our target images and the saturated images are the same size. The discriminator is a convolutional neural network consisting of eight convolutional layers and two fully connected (FC) layers. Each convolutional layer is followed by a batch normalization (BN) layer and a Leaky Rectified Linear Unit (LReLU) activation function layer, except for the first one. The generator and discriminator weighting are updated alternately until the end of training. The network training parameters are the same as the original network.<sup>17</sup> The learning rate was initialized as  $10^{-4}$ , and the models were trained on batch size of 4 for 150,000 iterations, performed on a server with NVIDIA TITAN RTX GPU and 64 GB RAM.

#### 2.4. Experiment system and datasets

A homemade OCT system<sup>18</sup> was used to collect data, whose light source is a super-light emitting diode (SLD) with a central wavelength of 840 nm and a bandwidth of 100 nm.

The phantom made of the mixture of AB liquid silica gel and polystyrene microspheres was used as the sample, and 25 pairs of clear-saturated image pairs were obtained as the training datasets, whose image size are 1000 pixels  $\times$  2048 pixels (width  $\times$  height), corresponding to the field of view of 3 mm ( $x$ )  $\times$  2.3 mm ( $z$ ).  $k$  was selected from 1 to 1.4 when simulating saturated images. The dataset was expanded by mirror flipping, and then each OCT image was empirically cropped to patches with 64 pixels  $\times$  64 pixels. After removing the black background sub-images, we obtained 11,391 and 11,525 small images in the experimental and simulated datasets, with 5% of the images randomly selected as the validation set and the others as the training set.

Further, the OCT images of zebrafish and human thyroid tissue, with rich texture structure and detailed information, were collected to test the OCT artifacts inpainting ability of the trained models.

#### 2.5. Quantitative metrics

Three common metrics, peak signal-to-noise ratio (PSNR), structural similarity index measure (SSIM), and learned perceptual image patch similarity (Lpips) were used to evaluate the results quantitatively.

As shown in Eq. (1), PSNR is calculated based on the error between corresponding pixels of two images  $I$  and  $I_{\text{ref}}$

$$\begin{aligned} \text{PSNR} &= 10 \log_{10} \left( \frac{\text{MAX}(I)^2}{\text{MSE}} \right), \\ \text{MSE} &= \frac{1}{hw} \sum_{x=1}^w \sum_{z=1}^h (I(x, z) - I_{\text{ref}}(x, z))^2, \end{aligned} \quad (1)$$

where  $\text{MAX}(I)$  represents the theoretical maximum of the pixel value in image  $I$  and  $h$ ,  $w$  are image height and width.

SSIM calculates the image similarity from luminance, contrast, and structure of the image  $I$  and reference image  $I_{\text{ref}}$  as follows:

$$\begin{aligned} \text{SSIM}(I, I_{\text{ref}}) &= l(I, I_{\text{ref}}) \cdot c(I, I_{\text{ref}}) \cdot s(I, I_{\text{ref}}) \\ l(I, I_{\text{ref}}) &= \frac{2\mu_I \mu_{I_{\text{ref}}} + C_1}{\mu_I^2 + \mu_{I_{\text{ref}}}^2 + C_1}, \\ c(I, I_{\text{ref}}) &= \frac{2\sigma_I \sigma_{I_{\text{ref}}} + C_2}{\sigma_I^2 + \sigma_{I_{\text{ref}}}^2 + C_2}, \\ s(I, I_{\text{ref}}) &= \frac{\sigma_{II_{\text{ref}}} + C_3}{\sigma_I \sigma_{I_{\text{ref}}} + C_3}, \end{aligned} \quad (2)$$

where  $l$ ,  $c$ , and  $s$  are functions of luminance, contrast, and structure, respectively. Here,  $\mu_I$  and  $\mu_{I_{\text{ref}}}$  are the mean intensities of images  $I$  and  $I_{\text{ref}}$ .  $\sigma_I$  and  $\sigma_{I_{\text{ref}}}$  are the variances of images  $I$  and  $I_{\text{ref}}$ .  $\sigma_{II_{\text{ref}}}$  is the covariance between image  $I$  and reference image  $I_{\text{ref}}$ .  $C_1 = (K_1 L)^2$ ,  $C_2 = (K_2 L)^2$ , and  $C_3 = C_2/2$ .  $L$  is the dynamic range of the image.  $K_1$  and  $K_2$  were set to 0.01 and 0.03.

Lpips is used for the objective assessment of image similarity by deep features across neural network architectures, thereby approximating human perception in visual similarity evaluation. A lower Lpips value indicates a greater degree of similarity between the two images.

### 3. Results

Inpainting results of saturation artifacts in phantom images of test datasets are shown in Fig. 4.

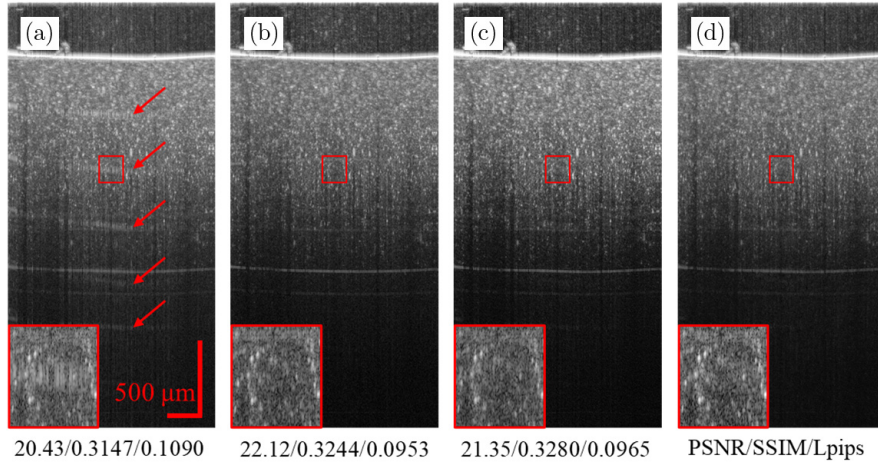


Fig. 4. Inpainting results of saturation artifacts in phantom OCT images. (a) and (b) are experimental saturated and clear OCT images. (c) and (d) are reconstructed images based on experimental and simulated trained models, respectively. The sub-image in the red boxes are magnified views of the selected area. The scale bar in the image is  $500 \mu\text{m}$ .

Figure 4(a) is an OCT image with saturation artifacts. Figure 4(b) is the clear OCT image. Figures 4(c) and 4(d) are the output results by experimental and simulated artifacts inpainting models, respectively. Meanwhile, the quantitative evaluation results are shown under the image in Fig. 4. As pointed by red arrows in Fig. 4(a), saturation artifacts like short vertical lines appear at different depths in OCT images because of strong backscattering. As shown in Figs. 4(c) and 4(d), the saturation artifacts are removed and the texture information masked by saturation artifacts is restored, proving the effectiveness of experimental and simulated artifacts inpainting models. The same conclusion is also demonstrated by the quantitative evaluation, where PSNR, SSIM, and Lpips were improved after inpainting.

Further, we tested the collected zebrafish images. Inpainting results of saturation artifacts in zebrafish spine OCT images are shown in Figs. 5(a<sub>1</sub>)–5(f<sub>1</sub>). As a comparison, the inpainting results of interpolation methods<sup>12</sup> are also shown in Fig. 5, in which they filled the pixels in the saturated area by interpolation adjacent unsaturated A-scans. Figure 5(a<sub>1</sub>) is an OCT image of zebrafish spine with saturation artifacts. Figures 5(b<sub>1</sub>) and 5(c<sub>1</sub>) are the output results of LI and spline interpolation (SI), respectively. Figures 5(d<sub>1</sub>) and 5(e<sub>1</sub>) are the results of experimental and simulated artifacts inpainting models, respectively. Figure 5(f<sub>1</sub>) is the clear OCT image collected experimentally.

Affected by bone structure and back undulation, saturation artifacts are easy to appear in zebrafish

OCT images, and display as close and consecutive artifacts. We can see that there are short vertical lines like saturation artifacts at different depths in the saturated image (Fig. 5(a<sub>1</sub>)), and they mask the true texture. In addition, the regions indicated by the red arrows are image artifacts due to strong autocorrelation from the strong scattering layer of the bone structure. The interpolation methods in Figs. 5(b<sub>1</sub>) and 5(c<sub>1</sub>) are LI and cubic SI, respectively. As shown in the corresponding enlarged red box area on the right of the images, artifacts cannot be effectively removed. Moreover, as shown in the areas of the yellow rectangular boxes of Figs. 5(b<sub>1</sub>) and 5(c<sub>1</sub>), we can see distorted and discontinuous texture structure, which means error information was introduced in the dense artifacts area, and caused local blurring and covered up the real texture structure. Therefore, LI and SI cannot achieve the effect of artifacts inpainting in this case of dense artifacts. Here, “dense” is a qualitative evaluation for the saturation. When there are close and consecutive artifacts in the image, we regard them as dense saturation. As shown in Figs. 5(d<sub>1</sub>) and 5(e<sub>1</sub>), the reconstructed images are nearly the same as the clear image (Fig. 5(f<sub>1</sub>)), and the saturation artifacts in the dense artifacts area and the deep sample area are both perfectly removed and the texture information are almost completely reconstructed.

Similarly, inpainting results of saturation artifacts in zebrafish tail OCT images are shown in Figs. 5(a<sub>2</sub>)–5(f<sub>2</sub>). Figure 5(a<sub>2</sub>) is an OCT image with saturation artifacts. Figures 5(b<sub>2</sub>) and 5(c<sub>2</sub>) are LI and SI results, respectively. Figures 5(d<sub>2</sub>) and 5(e<sub>2</sub>)

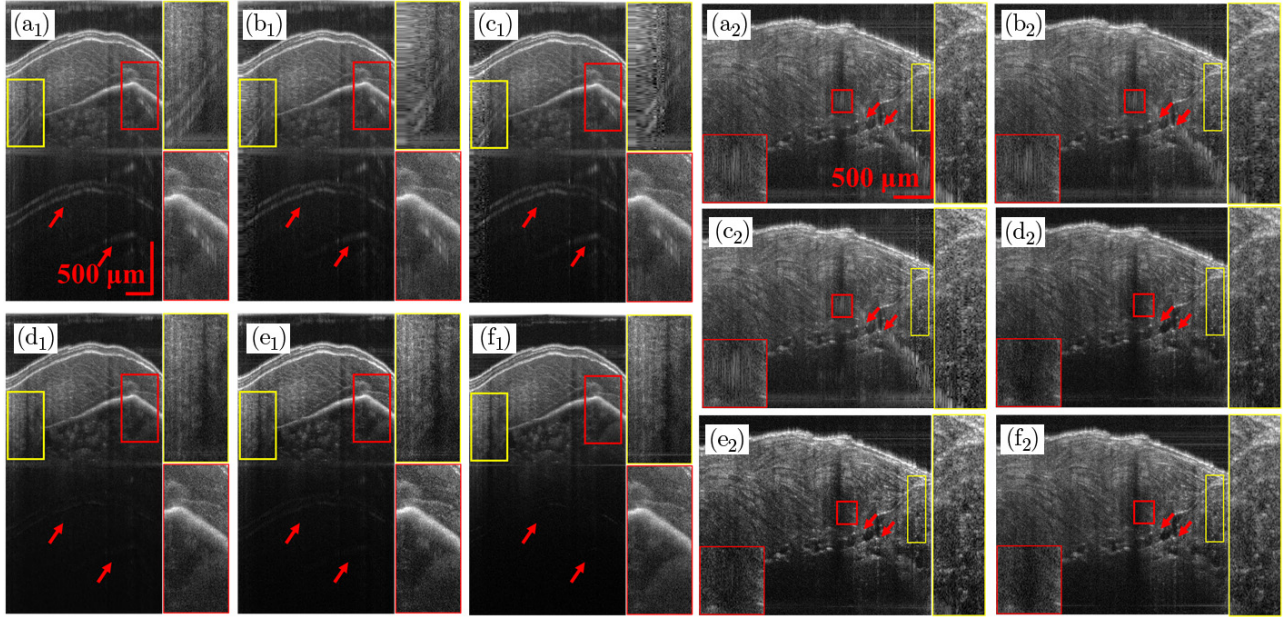


Fig. 5. Inpainting results of saturation artifacts in zebrafish spine and tail OCT images. (a<sub>1</sub>) is the experimental saturated zebrafish spine OCT image. (b<sub>1</sub>) is the output of LI. (c<sub>1</sub>) is the output of SI. (d<sub>1</sub>) and (e<sub>1</sub>) are output zebrafish spine images of experimental and simulated models, respectively. (f<sub>1</sub>) is the clear OCT image. (a<sub>2</sub>) is the experimental saturated zebrafish tail OCT image. (b<sub>2</sub>) is the output of LI. (c<sub>2</sub>) is the output of SI. (d<sub>2</sub>) and (e<sub>2</sub>) are zebrafish tail results of experimental and simulated models, respectively. (f<sub>2</sub>) is the clear OCT image. The right and the bottom-left sub-images are the magnified views of the selected corresponding areas. The scale bar in the image is 500  $\mu\text{m}$ .

are the results of experimental and simulated artifacts inpainting models, respectively. Figure 5(f<sub>2</sub>) is the clear OCT image. After inpainting, masked structures information was recovered by our proposed methods while the wrong textures were generated by LI and SI, which means that the deep learning-based inpainting methods are more effective.

The metrics on the 19 zebrafish test images are shown in Table 1. Interpolation in areas with dense saturation artifacts will introduce error information, and local blurring occurs near the artifacts area, so their quantitative results are lower than those of saturated images and clear images. In contrast, both the simulated and experimental models remarkably improved the image quality and achieved better average of SSIM, PSNR and Lpips, which is consistent with the visual effect of images

presented in Fig. 5. It should be noted that the test saturated image and its corresponding clear image were not collected simultaneously in experiments, so they didn't match completely, which means that the repaired image also doesn't match the clear image. PSNR and SSIM are calculated with corresponding pixels of images while Lpips measures the perceptual similarity without requiring pixel-to-pixel correspondence. Therefore, for PSNR and SSIM, we should focus on their relative changes rather than absolute values.

To show more applications in biological tissues, the inpainting results for the saturated OCT images of human thyroid tissue are shown in Fig. 6. Figure 6(a) is the experimental saturated OCT image. Figures 6(b) and 6(c) are the outputs of LI and SI, respectively, and Figs. 6(d) and 6(e) are the outputs of experimental and simulated inpainting

Table 1. Quantitative evaluation results of different methods.

	Saturated	Experimental	Simulated	LI	SI
PSNR	21.84	23.30	22.76	21.64	21.03
SSIM	0.2950	0.3151	0.3168	0.2715	0.2613
Lpips	0.1277	0.1261	0.1165	0.2356	0.2592

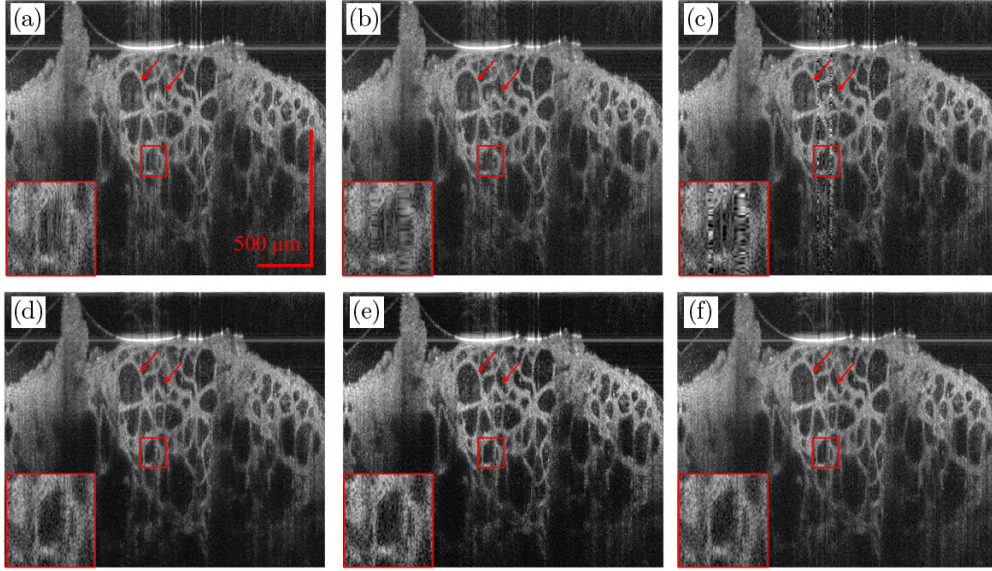


Fig. 6. Inpainting results of saturation artifacts in thyroid tissue OCT images. (a) and (f) are experimental saturated and clear OCT images, respectively. (b) is output of LI. (c) is output of SI. (d) and (e) are output images of our experimental and simulated models. The scale bar in the image is  $500\ \mu\text{m}$ .

models, respectively. Figure 6(f) is the corresponding clear OCT image. It can be found that the results of LI and SI are blurred, while our method can effectively remove the artifacts in the saturated images and reconstruct the texture information of spherical follicles in thyroid tissue.

#### 4. Discussions

Based on the generation mechanism, OCT images with saturation artifacts were acquired by experimental collection and digital simulation, and the clear-saturated image pairs were constructed as datasets to train ESRGAN and build artifacts inpainting models. Experimental results showed that both simulated and experimental image inpainting models can perfectly correct the artifacts in saturated images to obtain high visual quality. It proved the effectiveness of deep learning in OCT image inpainting of saturation artifacts. It is worth noting that the simulation method can be implemented without the limitation of sample collection and is more convenient and practicable.

Saturation artifacts usually occur and are inevitable in OCT imaging. Besides, the artifact may affect further tissue identification and classification in biological samples. Our work in this paper highlighted the wide-ranging potential of the deep learning-based inpainting methods. We think it can

be a preprocessing method of OCT imaging because of its high robustness and generalization.

To further study the rationality of the method, the error map of the output images and saturated images are provided in Fig. 7. Figures 7(a) and 7(b) are experimental saturated and clear OCT images, respectively. Figures 7(c) and 7(d) are output images from experimental and simulated models, respectively. The error maps were obtained by calculating the difference between the output images and saturated images. Figures 7(e) and 7(f) are error maps between corresponding output images and saturated images. As shown in the error maps, the main difference is the saturation artifacts, indicating that the trained model learns the difference in artifacts between images and does not alter the integrity of the original data.

More strikingly, only a single phantom sample was used to build the training dataset and train the ESRGAN to learn the correspondence between clear images and artifacts images in our study. In the meantime, we found the trained model can achieve great image inpainting effect in zebrafish and thyroid tissue samples, which proved the strong generalization ability of deep learning on this issue.

To remove saturation artifacts in the experimental collected OCT images, we proposed the deep learning-based method. Clear-saturated image pairs are required when training the model. The



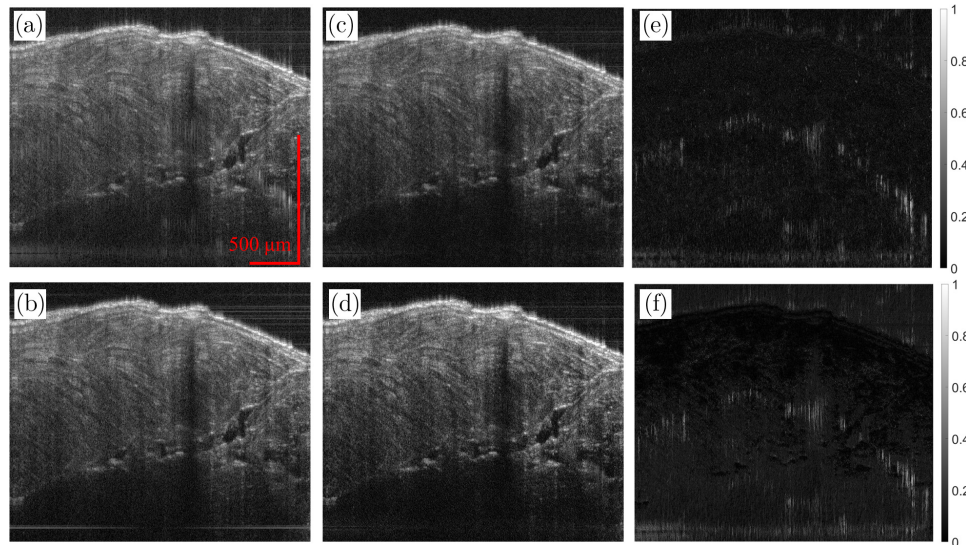


Fig. 7. Inpainting results of saturation artifacts in zebrafish OCT images. (a) and (b) are experimental saturated and clear OCT images, respectively. (c) is the output image of the experimental model. (d) is the output image of the simulated model. (e) is the error map between (a) and (c). (f) is the error map of (a) and (d). The scale bar in the image is  $500\ \mu\text{m}$ .

direct and effective method is to experimentally collect clear images and saturated images to construct the datasets. However, the experimental collection is complex and time-consuming. Therefore, we also tried the simulation method as an alternative and more efficient solution to construct datasets. The two models have the same network structures and were trained with the two sets of datasets, respectively. Finally, the experimental results showed that both models are effective for collected OCT images.

There are other noise and artifacts in OCT images, including complex conjugate-derived mirror images, artifacts from motion, irregular autocorrelation terms originating from the sample, and artifacts from coherence noise stripes of optical components. We will explore more application of deep learning in image inpainting for OCT images by analyzing and simulating noise and artifacts based on OCT imaging principles.

## 5. Conclusions

The feasibility of the deep learning-based inpainting of saturation artifacts in OCT images was proven by the reconstructed images, where the saturation artifacts were perfectly removed and the texture was almost completely reconstructed. The results of inpainting for different kinds of bio-tissue images showed its generalization and robustness.

Saturation artifacts are inevitable in OCT imaging. We think that deep learning-based inpainting can be used as a general preprocessing method for OCT images.


## Acknowledgments

Muyun Hu and Zhuoqun Yuan contributed equally to this work. This work was supported by the National Natural Science Foundation of China (62375144 and 61875092), Tianjin Foundation of Natural Science (21JCYBJC00260), and Beijing-Tianjin-Hebei Basic Research Cooperation Special Program (19JCZDJC65300).

## Conflicts of Interest

The authors declare that there are no conflicts of interest relevant to this paper.

## ORCID

Yanmei Liang  <https://orcid.org/0000-0002-8846-391X>

## References

1. R. F. Spaide, J. G. Fujimoto, N. K. Waheed, S. R. Sadda, G. Staurengi, “Optical coherence

- tomography angiography,” *Prog. Retin. Eye Res.* **64**, 1–55 (2018).
2. J. Tao, H. Chen, J. Yu, D. Cheng, Y. Chen, J. Mao, J. Fang, L. Shen, “Feasibility and utility of intraoperative optical coherence tomography during vitreoretinal surgery: A 4-year report in Chinese population,” *J. Innov. Opt. Health Sci.* **14**(1), 2140004 (2021).
  3. J. Olsen, J. Holmes, G. B. E. Jemec, “Advances in optical coherence tomography in dermatology — a review,” *J. Biomed. Opt.* **23**(4), 040901 (2018).
  4. Y.-J. Wang, J.-Y. Wang, Y.-H. Wu, “Application of cellular resolution full-field optical coherence tomography in vivo for the diagnosis of skin tumours and inflammatory skin diseases: A pilot study,” *Dermatology* **238**, 121–131 (2022).
  5. K. Nishimiya, G. Tearney, “Micro optical coherence tomography for coronary imaging,” *Front. Cardiovasc. Med.* **8**, 613400 (2021).
  6. Y. Wang, Y. Wan, Z. Chen, “Intravascular photoacoustic and optical coherence tomography imaging dual-mode system for detecting spontaneous coronary artery dissection: A feasibility study,” *J. Innov. Opt. Health Sci.* 2350016 (2023).
  7. F. LaRocca, S. J. Chiu, R. P. McNabb, A. N. Kuo, J. A. Izatt, S. Farsiu, “Robust automatic segmentation of corneal layer boundaries in SDOCT images using graph theory and dynamic programming,” *Biomed. Opt. Express* **2**(6), 1524–1538 (2011).
  8. J. Ouyang, T. S. Mathai, K. Lathrop, J. Galeotti, “Accurate tissue interface segmentation via adversarial pre-segmentation of anterior segment OCT images,” *Biomed. Opt. Express* **10**(10), 5291–5324 (2019).
  9. C.-T. Wu, M.-T. Tsai, C.-K. Lee, “Two-level optical coherence tomography scheme for suppressing spectral saturation artifacts,” *Sensors* **14**, 13548–13555 (2014).
  10. X. Li, S. Liang, J. Zhang, “Correction of saturation effects in endoscopic swept-source optical coherence tomography based on dual-channel detection,” *J. Biomed. Opt.* **23**(3), 030502 (2018).
  11. C.-K. Lee, M.-T. Tsai, C.-T. Wu, “A pseudo-spectrum reconstruction method for reducing saturation artifact in spectral-domain optical coherence tomography,” *Proc. Biophotonics: Photon. Solutions Better Health Care IV (SPIE, 2014)*, pp. 91290K.
  12. Y. Huang, J. U. Kang, “Real-time reference A-line subtraction and saturation artifact removal using graphics processing unit for high-frame-rate Fourier-domain optical coherence tomography video imaging,” *Opt. Eng.* **51**(7), 073203 (2012).
  13. H. Liu, S. Cao, Y. Ling, Y. Gan, “Inpainting for saturation artifacts in optical coherence tomography using dictionary-based sparse representation,” *IEEE Photon. J.* **13**(2), 3900110 (2021).
  14. Y. Ma, X. Chen, W. Zhu, X. Cheng, D. Xiang, F. Shi, “Speckle noise reduction in optical coherence tomography images based on edge-sensitive cGAN,” *Biomed. Opt. Express* **9**(11), 5129–5146 (2018).
  15. K. J. Halupka, B. J. Antony, M. H. Lee, K. A. Lucy, R. S. Rai, H. Ishikawa, G. Wollstein, J. S. Schuman, R. Garnavi, “Retinal optical coherence tomography image enhancement via deep learning,” *Biomed. Opt. Express* **9**(12), 6205–6221 (2018).
  16. Z. Yuan, D. Yang, H. Pan, Y. Liang, “Axial super-resolution study for optical coherence tomography images via deep learning,” *IEEE Access* **8**, 204941–204950 (2020).
  17. X. Wang, K. Yu, S. Wu, J. Gu, Y. Liu, C. Dong, Y. Qiao, C. C. Loy, “ESRGAN: Enhanced super-resolution generative adversarial networks,” *European Conference on Computer Vision (ECCV)* (Springer, 2018), pp. 1–16.
  18. D. Yang, Z. Yuan, Z. Yang, M. Hu, Y. Liang, “High-resolution polarization-sensitive optical coherence tomography and optical coherence tomography angiography for zebrafish skin imaging,” *J. Innov. Opt. Health Sci.* **14**(6), 2150022 (2021).
  19. X. Wang, L. Xie, C. Dong, Y. Shan, “Real-ESRGAN: Training real-world blind super-resolution with pure synthetic data,” *Proc. IEEE/CVF Int. Conf. Computer Vision (IEEE, 2021)*, pp. 1905–1914.
  20. K. Yamashita, K. Markov, “Medical image enhancement using super resolution methods,” *Computational Science — Int. Conf. Computational Science (ICCS)* (Springer, 2020), pp. 496–508.
  21. Y. Wang, G. Sun, S. Guo, “Target detection method for low-resolution remote sensing image based on ESRGAN and ReDet,” *Photonics* **8**, 431 (2021).